Double-Diffusive Convection in a Stochastic Shear

TIMOUR RADKO, JAMES BALL, JOHN COLOSI, AND JASON FLANAGAN

Department of Oceanography, Naval Postgraduate School, Monterey, California

ABSTRACT

An attempt is made to quantify the impact of stochastic wave–induced shears on salt fingers associated with internal waves in the ocean. The wave environment is represented by the superposition of Fourier components conforming to the Garrett–Munk (GM) spectrum with random initial phase distribution. The resulting time series of vertical shear are incorporated into a finger-resolving numerical model, and the latter is used to evaluate the equilibrium diapycnal fluxes of heat and salt. The proposed procedure makes it possible to simulate salt fingers in shears that are representative of typical oceanic conditions. This study finds that the shear-induced modification of salt fingers is largely caused by near-inertial motions. These relatively slow waves act to align salt fingers in the direction of shear, thereby rendering the double-diffusive dynamics effectively two-dimensional. Internal waves reduce the equilibrium vertical fluxes of heat and salt by a factor of 2 relative to those in the unsheared three-dimensional environment, bringing them close to the values suggested by corresponding two-dimensional simulations.

1. Introduction

This study examines the dynamics and transport characteristics of salt fingering in time-dependent vertical shears. Early discussions of double-diffusive convection (e.g., Stern 1969) often express concern that typical oceanic shears could be destructive for salt fingers. If proven valid, this suggestion would imply that the overall impact of double diffusion on water mass transformation and large-scale ocean dynamics is limited. This possibility motivated a number of investigations into finger–shear interactions, including laboratory studies (Linden 1974; Fernandes and Krishnamurti 2010), theoretical models (Kunze 1987, 1994), and numerical simulations (Kimura and Smyth 2007, 2011). These experiments alleviated earlier fears by demonstrating the resilience of fingers to dynamically stable shears. The vertical transport of heat and salt was shown to be only weakly dependent on the Richardson number $\text{Ri} = N^2/A_{sh}^2$, where N represents the buoyancy frequency and A_{sh} is the vertical shear. The dominant effect observed in the laboratory and numerical investigations was the alignment of temperature and

salinity perturbations in the direction of shear, resulting in the formation of so-called salt sheets. In the cross-flow direction, however, double diffusion was still realized in the form of vertically elongated filaments, similar to the patterns observed in nonsheared environments.

The question that arises at this point is whether the same quasi-two-dimensional conceptualization can be applied to salt fingers in the ocean. Oceanic shears are largely associated with internal waves and therefore they are neither steady nor unidirectional. Time dependence could lead to more substantial reduction in the intensity of double diffusion. As discussed in Kunze (1990) and Radko (2013), the perpetual change in the orientation of shear can potentially suppress fingering in all horizontal directions, not just one; this effect will be hereafter referred to as isotropic suppression.

The efficiency of isotropic suppression of fingers is determined by the time scales of shear. For instance, the dominant component of shear in the ocean is near inertial. It operates on the time scale of a day, whereas fingers grow and adjust to changes in the environment on a time scale of minutes. Given such a disparity of temporal scales, it is likely that the inertial shear can be viewed as quasi steady on finger scales. Internal waves operating on higher frequencies are less energetic, but their periods are closer to the finger time scales, and therefore the isotropic suppression could be more effective. The present investigation attempts to resolve

Corresponding author address: Timour Radko, Department of Oceanography, Naval Postgraduate School, 833 Dyer Rd., Room SP-344, Monterey, CA 93943.
E-mail: tradko@nps.edu

the uncertainty with regard to the effects of shear on fingers by considering the full spectrum of internal waves. The multifrequency time series of shear are constructed based on the empirical Garrett–Munk (GM) spectrum (Garrett and Munk 1972). These time series are incorporated into a small-scale direct numerical simulation (DNS) model, which, in turn, is used to evaluate the double-diffusive transport of heat and salt. Aside from some special regions of the World Ocean, which include high latitudes, very low latitudes, and coastal regions, the canonical GM spectrum is known to be representative of wave-induced variability (Munk 1981). Therefore, we expect that the GM-based model will provide some definitive answers regarding the finger–shear interaction.

2. Formulation and preliminary simulations

The proposed model contains two distinct components: (i) the DNS module used to simulate the evolution of salt fingers in the prescribed large-scale shear $[U_z(t), V_z(t)]$ and (ii) the internal wave module used to generate time series of the large-scale shear. The small-scale component (i) is analogous to the model used by Stern et al. (2001) and Radko (2003, 2014). The temperature and salinity fields (T_{tot}, S_{tot}) are separated into uniform vertical background gradients $(\overline{T}, \overline{S})$ and a departure (T, S) from it. Our focus is on finger-favorable background stratification $(\overline{T}_z > 0, \overline{S}_z > 0)$. The governing Boussinesq equations of motion are then expressed in terms of perturbations T and S. To reduce the number of controlling parameters, the system is non-dimensionalized using $d = [(k_T \nu)/(g\alpha\overline{T}_z)]^{1/4}$, k_T/d, d^2/k_T, and $(\rho_0 \nu k_T)/d^2$ as the scales of length, velocity, time, and pressure, respectively. Here, (k_T, k_S) denote the molecular diffusivities of heat and salt, ν is the viscosity, and ρ_0 is the reference density. The expansion–contraction coefficients (α, β) are incorporated in (T, S), and $\alpha\overline{T}_z d$ is used as the scale for both temperature and salinity perturbations. As a result, the governing equations reduce to

$$
\begin{cases}
\dfrac{\partial T}{\partial t} + \mathbf{v} \cdot \nabla T + w = \nabla^2 T \\[2mm]
\dfrac{\partial S}{\partial t} + \mathbf{v} \cdot \nabla S + \dfrac{w}{R_\rho} = \tau \nabla^2 S \\[2mm]
\dfrac{1}{\mathrm{Pr}} \left(\dfrac{\partial}{\partial t} \mathbf{v} + \mathbf{v} \cdot \nabla \mathbf{v} \right) = -\nabla p + (T - S)\mathbf{k} + \nabla^2 \mathbf{v} \\[2mm]
\nabla \cdot \mathbf{v} = 0
\end{cases}, \quad (1)
$$

where $R_\rho = (\alpha\overline{T}_{z\mathrm{dim}})/(\beta\overline{S}_{z\mathrm{dim}})$ is the background density ratio (the subscript "dim" here denotes dimensional quantities); $\tau = k_S/k_T$ is the diffusivity ratio; $\mathrm{Pr} = \nu/k_T$ is

the Prandtl number; $\mathbf{v} = (u, v, w)$ is the velocity vector; p is dynamic pressure; and $\mathbf{k}$ is the vertical unit vector. We assume periodic boundary conditions in each spatial direction and integrate the governing equations (1) using the dealiased pseudospectral method (e.g., Stern et al. 2001; Stellmach et al. 2011). The governing parameters for most simulations in this study are $(R_\rho, \mathrm{Pr}, \tau) = (2, 7, 0.01)$, which reflects representative conditions in the subtropical Atlantic thermocline, and the effects of variation in R_ρ are explored in section 3c.

The vertical shear is introduced into the model by prescribing the amplitude of the spectral component of (u, v) that is fundamental in z and uniform in (x, y)—the Fourier component (0, 0, 1). Several versions of the shear model have been considered, and we start our discussion by presenting preliminary single-frequency experiments. In our first set of simulations, the prescribed harmonic is given by

$$
\begin{cases}
u_{001} = A\cos(\omega t)\cos(mz) \\
v_{001} = -A\sin(\omega t)\cos(mz)
\end{cases}, \quad (2)
$$

where $m = 2\pi/L_z$ is the fundamental wavenumber in z. This system represents the shear flow that, at any given time, is unidirectional. In time, the basic current rotates at angular frequency ω, which allows us to examine the efficiency of isotropic suppression of fingers by shear. In the second version of the model, the prescribed harmonic represents the shear flow that rotates both in time and in space:

$$
\begin{cases}
u_{001} = A\cos(\omega t + mz) \\
v_{001} = -A\sin(\omega t + mz)
\end{cases}. \quad (3)
$$

The simulations were carried out in the computational domain of size $(L_x, L_y, L_z) = (50, 50, 100)$ that, assuming typical midlatitude stratification of $\overline{T}_z \sim 0.01°\mathrm{C\,m}^{-1}$, corresponds to dimensional values of $0.5\,\mathrm{m} \times 0.5\,\mathrm{m} \times 1\,\mathrm{m}$. The numerical mesh contained $(N_x, N_y, N_z) = (384, 384, 768)$ grid points. Doubling the resolution in selected runs to $(N_x, N_y, N_z) = (768, 768, 1536)$ had minimal effect (less than 4%) on the vertical transport of heat and salt, indicating that fingers are adequately resolved. Likewise, doubling the vertical size of the computational domain to $L_z = 200$, while maintaining the maximal magnitude of shear also changed the average fluxes by 4%.

With regard to the selection of the domain size, it should be mentioned that there is a critical condition that should be met in all DNS of double-diffusive convection. The amplitude equilibration of salt fingers occurs (e.g., Radko and Smith 2012) largely through their interaction with secondary instabilities (Holyer 1984). Thus, the choice of the domain will not affect salt-finger dynamics only as long as its vertical extent greatly
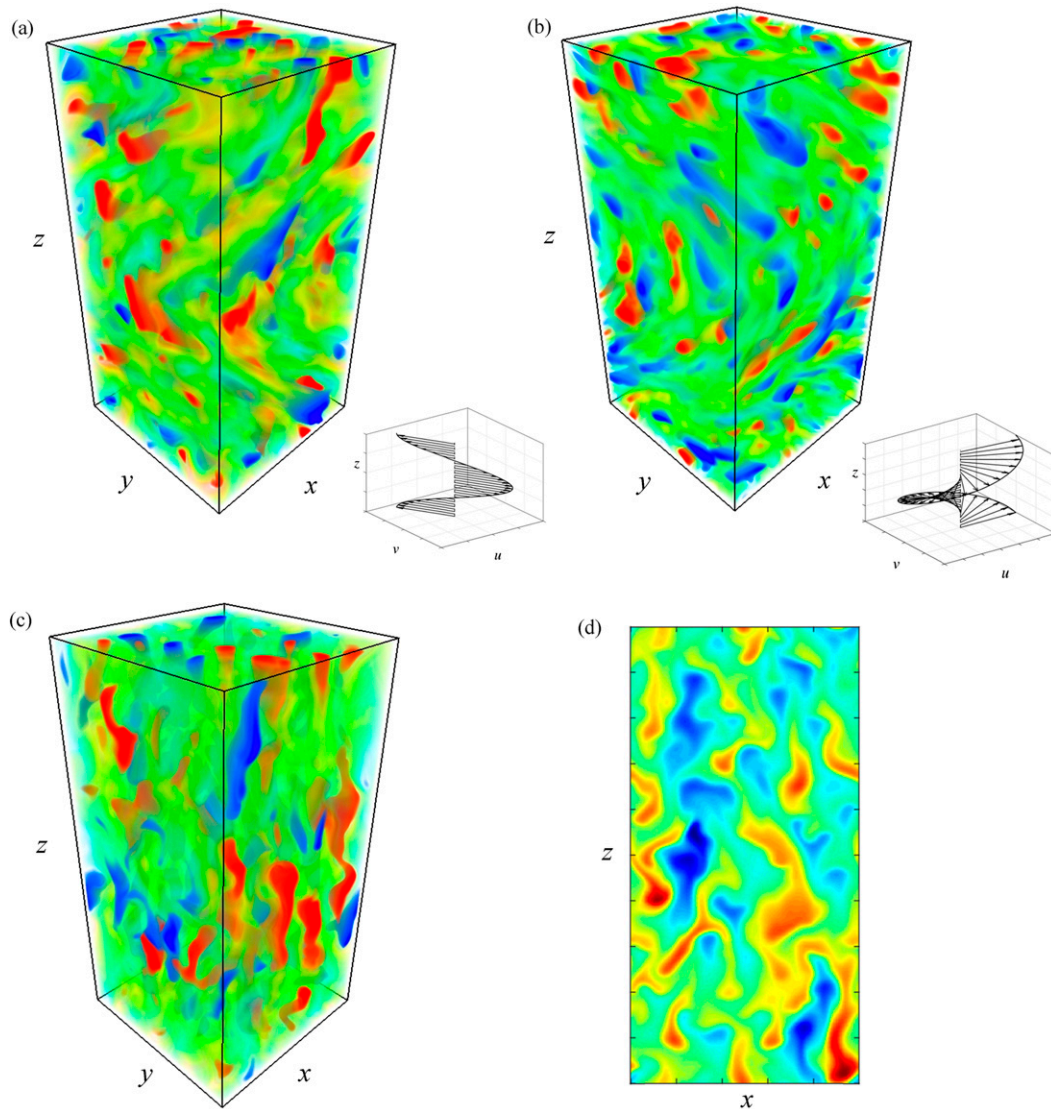
FIG. 1. Typical patterns of T (departure of temperature from the linear background gradient) in the following experiments: the simulations with (a) spatially unidirectional and (b) spatially rotating shear; the nonsheared (c) three-dimensional and (d) two-dimensional simulations. The background flow structure in (a) and (b) is illustrated in the inserts and the shear parameters are $\omega = 0.1\pi$ and Ri = 2. Red color corresponds to high values of T, and low values are shown in blue. The domain size is $(L_x, L_y, L_z) = (50, 50, 100)$ in nondimensional units.

exceeds the wavelength of the Holyer modes. Our simulations readily satisfy this condition. The vertical wavelength of the fastest growing Holyer instability for the parameter regime explored in the present study is $l_H \sim 15$, which is less than the domain height $L_z = 100$ used in most simulations.

Typical patterns realized in the single-frequency simulations are shown in Fig. 1 (the inserts indicate the structure of the prescribed shears). The spatially unidirectional shear (Fig. 1a) and the shear rotating both in space and in time (Fig. 1b) influence salt fingers in a similar manner. In both cases, there is an apparent

tendency to tilt salt fingers in the local direction of shear. In this regard, the model solutions differ considerably from the corresponding patterns realized in the nonsheared three-dimensional (Fig. 1c) and two-dimensional (Fig. 1d) simulations. The experiments in Figs. 1a and 1b were performed for the shear amplitude $A = 21.05$, which corresponds to the minimal Richardson number of Ri = 2 and the nondimensional frequency of $\omega = 0.1\pi$ (equivalent to the dimensional period of $t_{\text{dim}} \approx$ 4 h). However, the qualitative features revealed by simulations in Fig. 1 are sufficiently generic and not sensitive to variation in governing parameters.
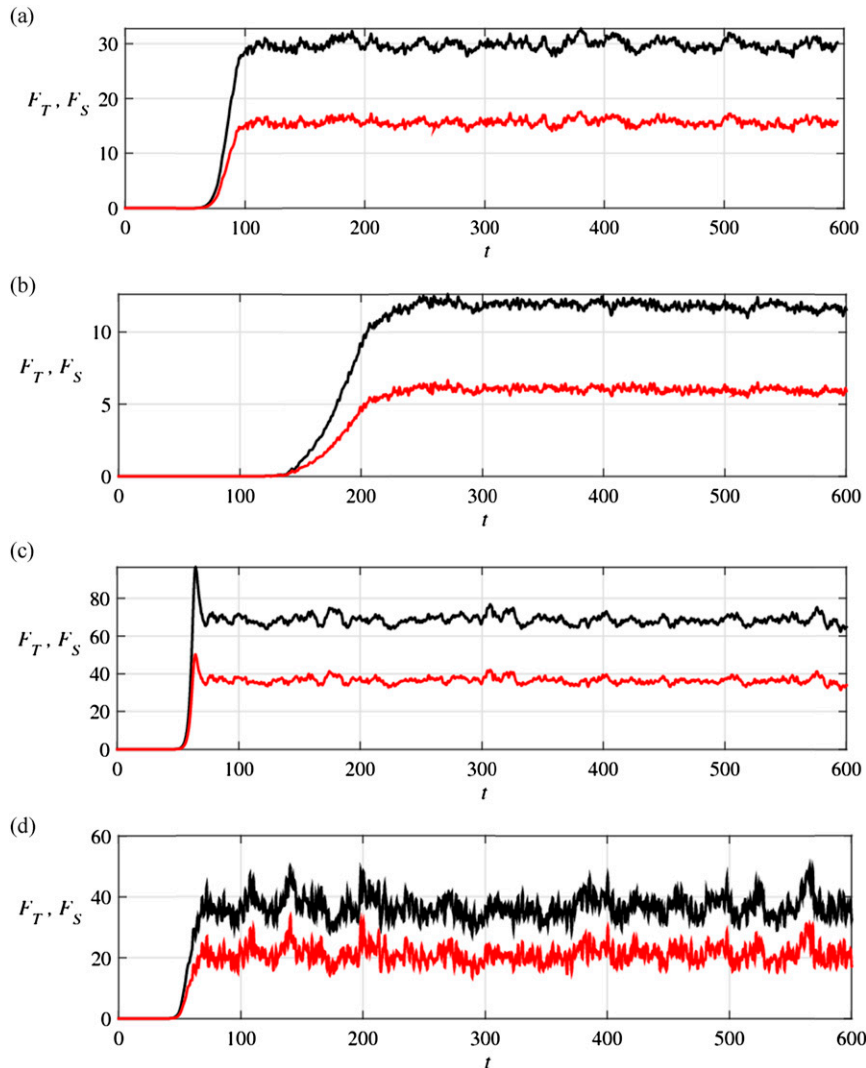
FIG. 2. (a)–(d) The time records of fluxes for the experiments in Figs. 1a–d, respectively. The
red (black) curves represent the temperature (salinity) fluxes.

Figure 2 presents the time series of the spatially averaged downward fluxes of heat and salt $(F_T, F_S) = (-\overline{wT}, -\overline{wS})$ for the experiments in Fig. 1. In all cases, the fluxes grow exponentially during the linear phase of the fingering evolution but ultimately equilibrate, reaching a statistically steady regime with well-defined mean values. Despite the considerably different geometry of shear in Figs. 1a and 1b, the resulting fluxes are comparable as indicated in Table 1, which summarizes all simulations presented in this study. The experiments with spatially rotating shear (e.g., Fig. 1b) produced larger fluxes relative to the experiments with temporal variability only (e.g., Fig. 1a) for $\omega = 0.8\pi$ and weaker fluxes for other frequencies considered. The limited sensitivity of fluxes to the shear pattern is encouraging since it reduces the uncertainty in terms of

application of our results to the ocean. We should also add that the spatial variability in the direction of the background flow in Fig. 1b (where the vertical scale is $\sim$1 m) is unrealistically high. Thus, its inability to strongly influence the vertical transport in our simulations suggests that the effects of changing flow direction with depth in the ocean are even less. Therefore, the shear model adopted in the subsequent section will be the one with spatially uniform (albeit temporally variable) flow direction.

3. Salt fingers in a stochastic shear

A natural step in the development of a realistic description of finger–shear interaction is to incorporate shear that is representative of the real ocean. In this

TABLE 1. Integral mixing characteristics of salt fingers evaluated at the quasi-equilibrium stage are summarized for the experiments presented in section 2 (single-frequency and nonsheared DNS). The second and third columns list the mean nondimensional downward turbulent fluxes of heat and salt $F_T = -\overline{wT}$ and $F_S = -\overline{wS}$, where the averages are taken over the entire volume of the computational domain and in time, over the period of quasi-equilibrium evolution. The fourth and fifth columns are the corresponding dimensional diffusivities of heat and salt. The sixth column is the corresponding dimensional heat flux evaluated for $\overline{T}_z \sim 0.01°C\,m^{-1}$.

Preliminary experiments	F_T	F_S	$K_{T\mathrm{dim}} = F_T k_T \times 10^{-6}\,m^2\,s^{-1}$	$K_{S\mathrm{dim}} = F_S k_T R_\rho \times 10^{-6}\,m^2\,s^{-1}$	$F_{H\mathrm{dim}} = c_p \rho k_T \overline{T}_z F_T$ W m^{-2}
			Nonsheared		
2D (Figs. 1d, 2d)	22.809	39.169	3.193	10.966	0.1373
3D (Figs. 1c, 2c)	36.482	68.579	5.108	19.202	0.2197
			Single-frequency, parallel shear [(2)]		
$\omega = 0$	16.542	31.086	2.316	8.704	0.0996
$\omega = 0.1\pi$ ($t_{\mathrm{dim}} = 4\,h$)	15.527	29.429	2.174	8.239	0.0939
$\omega = 0.1\pi$ $L_z = 200$	16.142	30.539	2.260	8.551	0.0972
$\omega = 0.2\pi$ ($t_{\mathrm{dim}} = 2\,h$)	15.133	29.918	2.119	8.377	0.0911
$\omega = 0.4\pi$ ($t_{\mathrm{dim}} = 1\,h$)	15.374	29.333	2.152	8.2132	0.0926
$\omega = 0.8\pi$ ($t_{\mathrm{dim}} = 0.5\,h$)	15.726	29.933	2.202	8.381	0.0947
			Single-frequency, rotating shear [(3)]		
$\omega = 0$	8.091	15.492	1.127	4.327	0.0485
$\omega = 0.1\pi$ ($t_{\mathrm{dim}} = 4\,h$)	6.073	11.950	8.502	3.346	0.0366
$\omega = 0.2\pi$ ($t_{\mathrm{dim}} = 2\,h$)	10.391	18.636	1.454	5.218	0.0626
$\omega = 0.4\pi$ ($t_{\mathrm{dim}} = 1\,h$)	14.995	27.415	2.099	7.676	0.0903
$\omega = 0.8\pi$ ($t_{\mathrm{dim}} = 0.5\,h$)	27.315	49.128	3.8241	1.376	0.1645

regard, it is essential that spectral characteristics of the imposed background flow are consistent with the variability of the internal waves in the ocean. Our procedure for constructing the time series of shear is based on the Garrett–Munk spectrum. The method for computing the random realizations of shear follows directly the treatments of Colosi and Brown (1998) and Sun and Kunze (1999) and will be briefly summarized below.

a. Formulation

The large-scale calculation is performed in the dimensional form. The shear is modeled from a superposition of internal waves whose energy distribution obeys the Garrett–Munk internal wave spectral model (Munk 1981). The horizontal currents as a function of depth and time are thus written as a linear sum of waves with different mode numbers j and horizontal wavenumbers k and l:

$$U_{\mathrm{dim}}(z,t) = \mathrm{Re}\left\{ \sum_{j=1}^{J} \int\int a_u(k,l,j)\cos[m(j)z]e^{i[\theta_u(k,l,j)-\sigma t]}\,dk\,dl \right\}$$

$$V_{\mathrm{dim}}(z,t) = \mathrm{Re}\left\{ -\sum_{j=1}^{J} \int\int a_v(k,l,j)\cos[m(j)z]e^{i[\theta_v(k,l,j)-\sigma t]}\,dk\,dl \right\}. \quad (4)$$

Here, the current modes are given by $\cos[m(j)z]$, where $m(j) = \pi j/D$, with water depth $D = 1000$ m; $\tan\theta_u = fl/(-\sigma k)$; and $\tan\theta_v = fl/(\sigma k)$, with Coriolis parameter $f = 7.27 \times 10^{-5}\,s^{-1}$. We assume uniform stratification with buoyancy frequency $N = \sqrt{g\alpha\overline{T}_z(1 - R_\rho^{-1})}$, and the Wentzel–Kramers–Brillouin (WKB) dispersion relation is given by

$$\sigma(k,l,j) = \sqrt{f^2 + N^2\frac{k^2+l^2}{m^2}}. \quad (5)$$

The stochastic wave amplitudes a_u and a_v are zero-mean complex Gaussian random variables that have variance given by the Cartesian GM spectra:

$$F_u(k,l,j) = F_\zeta(k,l,j)\frac{m^2(j)}{k^2+l^2}f^2(1 + k^2/\hat{k}_j^2)$$

$$F_v(k,l,j) = F_\zeta(k,l,j)\frac{m^2(j)}{k^2+l^2}f^2(1 + l^2/\hat{k}_j^2), \quad (6)$$

with

$$F_\zeta(k,l,j) = \zeta_o^2\frac{1}{N_j}\frac{1}{j^2+j_*^2}\frac{2}{\pi^2}\frac{\hat{k}_j\sqrt{k^2+l^2}}{k^2+l^2+\hat{k}_j^2}. \quad (7)$$

Here, ζ_o is the rms internal wave displacement. The displacement variance is related to the more traditional (nondimensional) energy norm $E = 6.3 \times 10^{-5}$, which for the constant N case is given by $\zeta_o^2 = ED^2/2$. The term
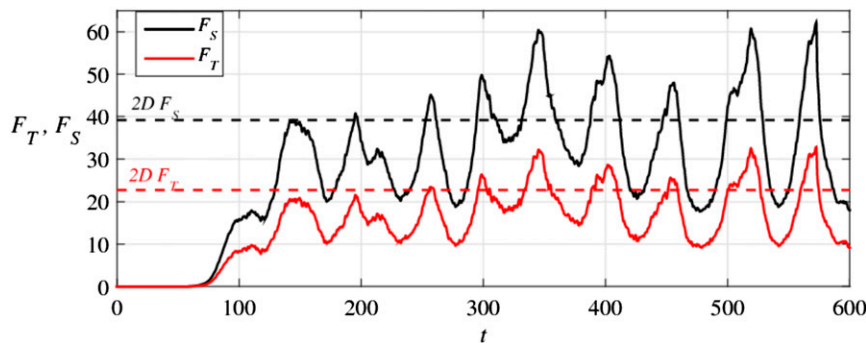
FIG. 3. The time record of temperature (solid red) and salinity (solid black) fluxes for the simulation with the GM-derived shear. Dashed lines represent the corresponding average fluxes for the two-dimensional nonsheared simulation.

N_j in (7) is a normalization defined through $N_j^{-1}\sum_{j=1}^{J}(j^2 + j_*^2)^{-1} = 1$, and $\hat{k}_j = m(j)f/N$. Our simulations are based on canonical GM parameters, that is, $\zeta_o = 7.3$ m and $j_* = 3$ (Munk 1981). The summation in (4) is over wavenumber and mode number contributions with amplitudes a_u and a_v having the variances $F_u dkdl$ and $F_v dkdl$. The WKB dispersion relation can assign waves frequencies above N, and in these cases the wave amplitudes a_u and a_v are set to zero. An important quantity is the maximum mode number J that controls the strength of shear. This wavenumber is related to the target Richardson number based on time-mean shear variance

$$\text{Ri}_{\text{mean}} = \frac{N^2}{U_z^2 + V_z^2} \qquad (8)$$

by $J = D^2/(6\text{Ri}_{\text{mean}}\pi\zeta_o^2 j_*^2)$. Using (4), the shear was evaluated at $z = 500$ m and recorded for the time period of $0 < t < t_f$, where $t_f = 4$ days, which is the time scale chosen as a trade-off between numerical feasibility and the requirement to resolve the inertial frequency. To ensure that a particular random realization matches the target Richardson number exactly, the resulting shear values were postprocessed by renormalizing their amplitudes accordingly.

Next, the time series of shear were nondimensionalized and incorporated into the small-scale model using

$$\begin{cases} u_{001} = A_u(t)\cos(mz) \\ v_{001} = A_v(t)\cos(mz) \end{cases}, \qquad (9)$$

where the velocity amplitude (A_u, A_v) is determined, at any instant of time, by the shear $[U_z(t), V_z(t)]$ generated by the large-scale GM-based model. One can easily recognize that system (9) represents the multifrequency generalization of model (2) used for the experiments in section 2. Aside from a more realistic temporal record of shear, the setup of DNS in this section is analogous to that in section 2.

b. A representative example

The dynamics of finger–shear interaction is largely controlled by two key nondimensional parameters: the Richardson number based on time-mean shear variance Ri_{mean} and the density ratio R_ρ. Before embarking on the exploration of the parameter space, we first examine a representative case $(\text{Ri}_{\text{mean}}, R_\rho) = (1, 2)$ in some detail.

Figure 3 presents the time record of T–S fluxes resulting from the simulation based on the GM shear. As previously (e.g., Fig. 2), fluxes first amplify exponentially. However, by $t \sim 300$ the system enters the statistically steady regime characterized by irregular oscillations of fluxes about their respective equilibrium values. Importantly, these equilibrium values are very close to the fluxes obtained from the nonsheared 2D simulations (Fig. 2d) and are considerably less than the corresponding 3D values (Fig. 2c). This observation suggests that even in the stochastic wave environment, with shear direction irregularly varying in time, the essential dynamics of salt fingering is quasi two-dimensional.

The effective homogenization in the direction of shear is also revealed by the inspection of horizontal cross sections of properties. For instance, Figs. 4a–c present salinity distributions realized at various instances of time at $z = \frac{1}{4}L_z$, the location of maximal shear. These patterns consist of elongated filaments generally aligned in the direction of shear (indicated by black arrows). The solutions in Figs. 4a–c are contrasted with the predominantly isotropic salinity patterns obtained in the corresponding three-dimensional nonsheared simulation (Fig. 4d).

It is important to emphasize that while the 2D nonsheared model is consistent with the long-term time-averaged T–S transport, the temporal variability of (F_T, F_S) is apparently affected by the variation in shear
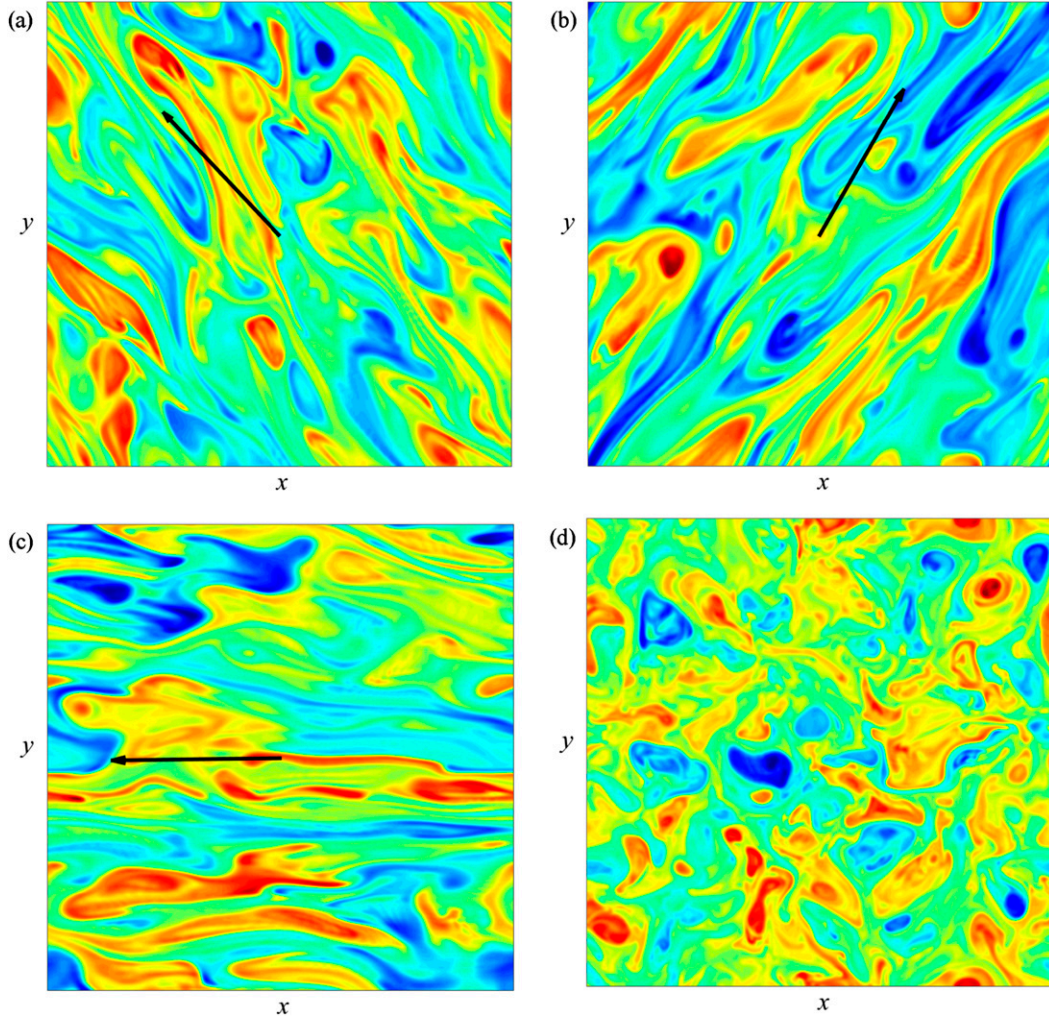
FIG. 4. (a)–(c) Horizontal cross section of salinity at the location of maximal shear $S(x, y, \frac{1}{4}L_z)$ at various times. Black arrows indicate the direction of shear. (d) A typical salinity cross section in the nonsheared experiment.

strength. This feature is illustrated (Fig. 5) by presenting time records of the relative variation of heat flux with respect to the mean value,

$$r_{\mathrm{fl}} = \frac{F_T - \overline{F}_T}{\overline{F}_T}, \tag{10}$$

and of the relative variation in the absolute value of shear,

$$r_{\mathrm{sh}} = \frac{A_{\mathrm{sh}} - \overline{A}_{\mathrm{sh}}}{\overline{A}_{\mathrm{sh}}}, \tag{11}$$

where $A_{\mathrm{sh}} = \sqrt{U_z^2 + V_z^2}$. The time record of flux variation $r_{\mathrm{fl}}(t)$ is plotted in Fig. 5 along with $-r_{\mathrm{sh}}(t)$. Remarkably, after the initial period of adjustment, these quantities become strongly correlated ($r_{\mathrm{fl}} \approx -r_{\mathrm{sh}}$). The

increase (decrease) in shear triggers an almost instantaneous reduction (amplification) of the vertical heat transport. Thus, the conclusion that we can draw from these simulations is somewhat counterintuitive. While the time-mean double-diffusive fluxes may not be particularly sensitive to the magnitude of shear, their instantaneous values are.

Finally, it is of interest to assess the impact of various spectral components of shear on salt fingers. This was accomplished by separating the frequency range of internal waves $f < \omega < N$ into three regions: (i) the low-frequency range $\omega < f_1$, (ii) the intermediate-frequency range $f_1 < \omega < f_2$, and (iii) the high-frequency range $\omega > f_2$. The dividing frequencies f_1 and f_2 are chosen as follows:

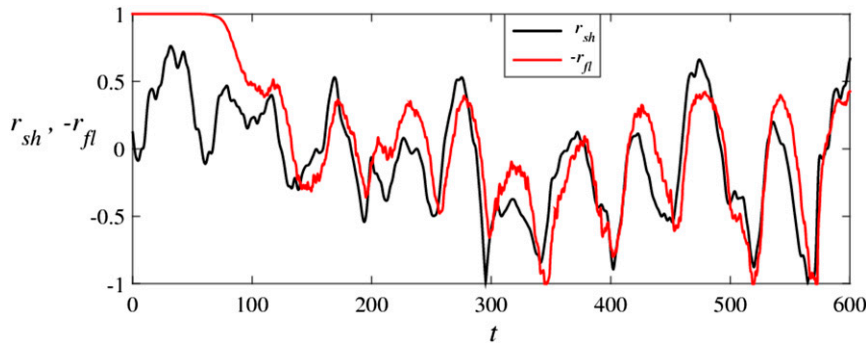$$f_1 = f + 0.1(N - f), \quad f_2 = f + 0.25(N - f). \tag{12}$$

FIG. 5. The relative variation of temperature flux with respect to the time-averaged value r_{fl} is plotted as a function of time along with $-r_{sh}$, where r_{sh} is the corresponding relative variation in the shear strength.

The shear components defined in this manner were extracted by Fourier transforming the time series of shear into the frequency domain and retaining only the harmonics in the corresponding frequency range. For each of the filtered time series, we have performed a small-scale DNS, and the time records of fluxes in these simulations are shown in Fig. 6. The most striking result in this figure is that neither high- nor intermediate-frequency components of shear have much impact on the intensity of fingering. The time-mean flux values in these experiments are much closer to their nonsheared 3D counterpart (Fig. 2c) than to the fluxes recorded in the original experiment (Fig. 3). The fluxes in the low-frequency simulation, on the other hand, are similar to the nonfiltered experiment (Table 2).

The three-dimensional patterns realized in the GM-based calculations (Fig. 7) support our view of high-frequency shear components as being too weak and low-frequency components as being too slow to isotropically suppress fingers. The unfiltered (Fig. 7a) and low-frequency (Fig. 7b) simulations are both characterized by strong tilt of salt fingers by the large-scale shear. In contrast, the patterns in the intermediate (Fig. 7c) and high-frequency (Fig. 7d) experiments retain the vertically elongated structure reminiscent of unsheared 3D simulations (e.g., Fig. 1c).

c. Exploration of the parameter space

An attempt has also been made to analyze the response of our system to the variation in governing parameters (Ri_{mean}, R_ρ). We performed a series of experiments in which the Richardson number and the density ratio were systematically varied within the limits

$$0.5 < Ri_{mean} < 4$$
$$1.5 < R_\rho < 2.5. \tag{13}$$

For the reasons given below, we believe that (13) is likely to capture most of the oceanographically relevant parameter range.

While the choice of the appropriate range of Ri_{mean} is far from obvious, some crude estimates could be made on the basis of oceanographic measurements of the instantaneous Richardson number Ri_{inst}. These observations (e.g., Monin and Ozmidov 1985; Polzin et al. 2003) typically indicate that dynamic instabilities ($Ri_{inst} < \frac{1}{4}$) in the open ocean are relatively rare. For instance, the so-called intermittency coefficient I that measures the fraction of the volume occupied by turbulence at any given time is on the order of $I \sim 5\%$. The time records of Ri_{inst} generated by our GM-based model suggest that the calculation presented in section 3b generally conforms to this requirement. For $Ri_{mean} = 1$, the dynamically unstable periods ($Ri_{inst} < \frac{1}{4}$) constitute only 2.8% of the record. The reduction of the Richardson number to $Ri_{mean} = 0.5$ raises this fraction to 10.2%, while the
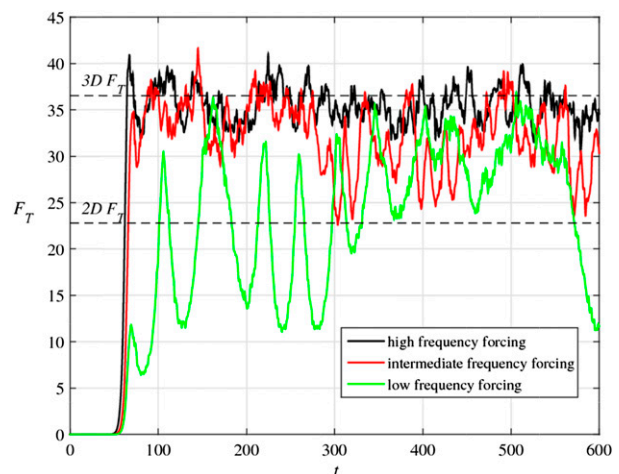

FIG. 6. The time records of temperature fluxes in the filtered experiments, which take into account only the low-frequency (green), intermediate-frequency (red), and high-frequency (black) components of the full GM spectrum of shear. The horizontal dashed lines represent the equilibrium fluxes realized in the three-dimensional and two-dimensional nonsheared experiments.

TABLE 2. As in Table 1, but for the GM-based simulations (section 3).

GM-based experiments	R_ρ	$\mathrm{Ri_{mean}}$	F_T	F_S	$K_{Tdim} = F_T k_T \times 10^{-6}\,\mathrm{m^2\,s^{-1}}$	$K_{Sdim} = F_S k_T R_\rho \times 10^{-6}\,\mathrm{m^2\,s^{-1}}$	$F_{Hdim} = c_p \rho k_T \overline{T}_z F_T \ \mathrm{W\,m^{-2}}$
Full spectrum	2	1	16.807	32.027	2.353	8.968	0.1012
Low frequency	2	1	23.391	44.510	3.275	1.246	0.1408
Midfrequency	2	1	32.134	61.030	4.499	1.709	0.1935
High frequency	2	1	35.441	66.997	4.962	1.875	0.2134
Full spectrum	1.5	1	34.183	60.944	4.786	12.80	0.2058
Full spectrum	1.75	1	24.775	45.993	3.469	11.29	0.1492
Full spectrum	2.25	1	7.650	14.923	1.071	4.701	0.0461
Full spectrum	2.5	1	4.365	8.667	0.611	3.033	0.0263
Full spectrum	2	0.5	8.512	16.207	1.192	4.538	0.0513
Full spectrum	2	2	17.460	33.243	2.444	9.308	0.1051
Full spectrum	2	4	18.358	35.063	2.5701	9.818	0.1105

increase of $\mathrm{Ri_{mean}}$ above 2 effectively precludes the dynamic destabilization (Fig. 8). These values suggest that our baseline experiment in section 3b is generally representative of oceanic conditions, while $\mathrm{Ri_{mean}} = 0.5$ ($\mathrm{Ri_{mean}} = 2$) corresponds to the levels of shear that are higher (lower) than the average.

It is interesting to examine the effects of the variation in $\mathrm{Ri_{mean}}$ on the salt-finger transport (Table 2). The increase in $\mathrm{Ri_{mean}}$ to 2 and 4 relative to the baseline experiment (section 3b) has very small (~10%) impact on the T–S fluxes. However, for $\mathrm{Ri_{mean}} = 0.5$, the finger fluxes diminish by a factor of 2. What makes this experiment unique among other simulations in this study (Table 2) is the extended presence of dynamic instabilities that are expected to produce substantial levels of turbulence (Fig. 8). Therefore, it is perhaps more appropriate to attribute the reduction of T–S fluxes in the $\mathrm{Ri_{mean}} = 0.5$ case to the suppression of fingers by the mechanically generated turbulence (e.g., Wells and Griffiths 2003; Smyth and Kimura 2011) rather than to the direct effects of shear, which is the primary objective of our study. The general conclusion that we draw from this analysis is that finger-driven transport is not particularly sensitive to the chosen $\mathrm{Ri_{mean}}$ as long as it is realistically high.

The focus on the density ratio range in (13) can be rationalized by noting that the density ratios below $R_\rho = 1.5$ are relatively rare (e.g., You 2002) and the density ratios above $R_\rho = 2.5$ result in weak fluxes that are probably not very significant for large-scale dynamics (e.g., St. Laurent and Schmitt 1999). The experimentation with various values of R_ρ resulted in solutions that are qualitatively similar, although there is an apparent tendency for salt fingering to intensify with the decreasing density ratio. This trend is readily confirmed by Fig. 9, which shows the mean equilibrium temperature fluxes plotted as a function of R_ρ. To determine whether the effective two-dimensionalization by shear occurs in

the entire set of simulations, these results are superimposed on the extant parameterizations of two-dimensional nonsheared salt fingers (Stern et al. 2001; Simeonov and Stern 2004; Radko 2014). The fluxes in the stochastic shear generally follow the pattern of $F_T(R_\rho)$ realized for nonsheared 2D fingers. While the stochastic fluxes tend to be less (by ~20%–30%) than their two-dimensional counterparts, the discrepancy is comparable to the uncertainties in 2D parameterizations. Furthermore, some reduction in finger intensity is also expected due to the intermittent dynamic destabilization and associated turbulence production, which has an adverse effect on double-diffusive transport (e.g., Smyth and Kimura 2011). Both 2D and stochastically sheared experiments, however, differ substantially from the corresponding three-dimensional nonsheared simulations (e.g., Radko and Smith 2012) that result in fluxes that are offset relative to the data in Fig. 9 by a factor of 2–3.

4. Discussion

This study attempts to describe the dynamics and transport characteristics of salt fingering in time-dependent vertical shears associated with internal waves in the ocean. The wave environment is represented by the superposition of Fourier components conforming to the Garrett–Munk (GM) spectrum with random initial phase distribution. The resulting time series of shear are then incorporated into the small-scale DNS. Based on these simulations, we draw the following conclusions:

1) The dominant effect observed in the GM-based simulations is that of alignment of temperature and salinity perturbations in the direction of shear and the formation of salt sheets. These effects have been previously observed in experiments with unidirectional shears (Linden 1974; Kimura and Smyth 2007;
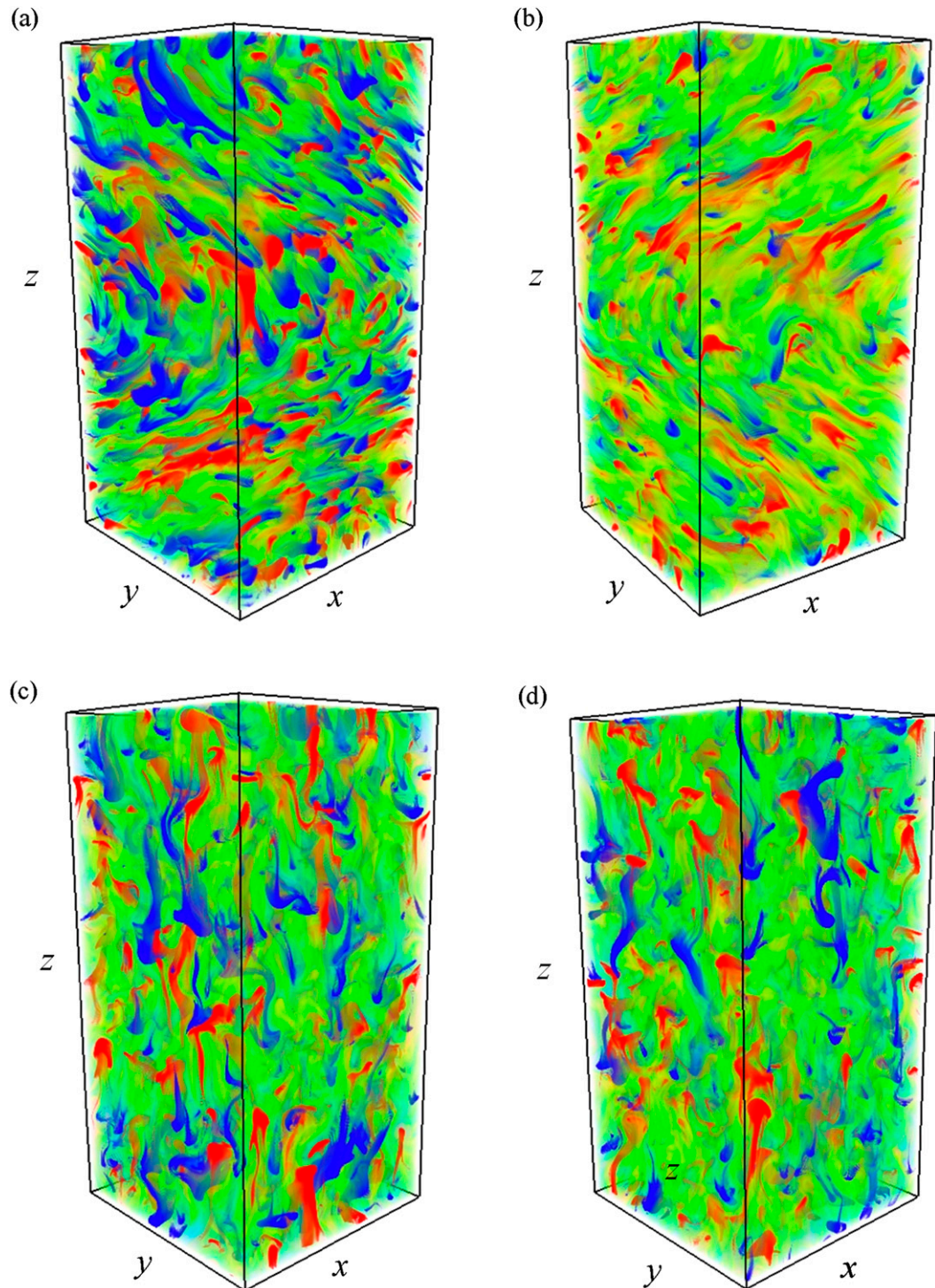
FIG. 7. Typical patterns of S (departure of salinity from the linear background gradient) in the GM-based experiments. The shear computed from the full GM spectrum of internal waves is shown in (a). The filtered experiments, which take into account only the (b) low-, (c) intermediate-, and (d) high-frequency components of the full GM spectrum. Red color corresponds to high values of S and low values are shown in blue. The domain size is (L_x, L_y, L_z) = (50, 50, 100) in nondimensional units.
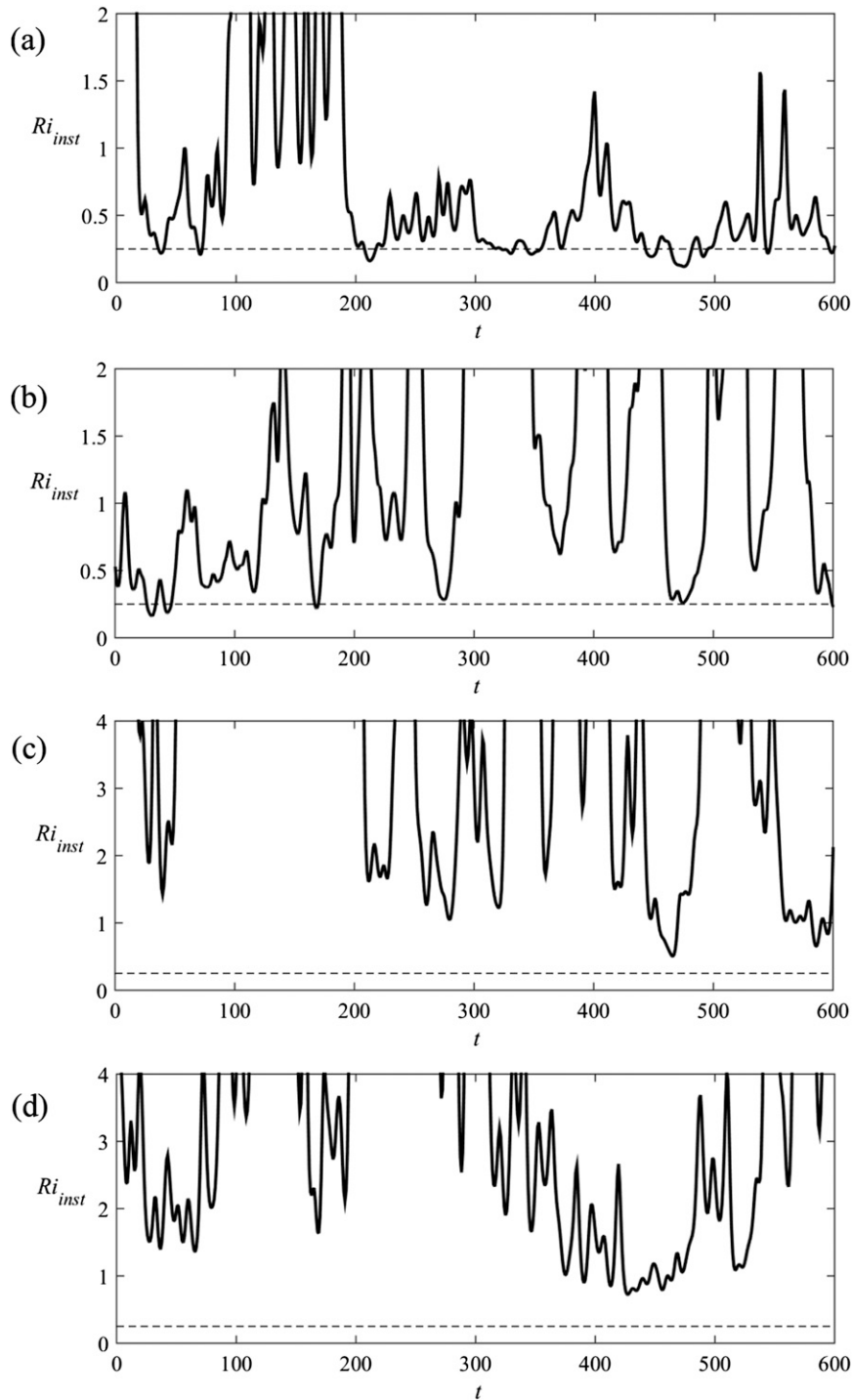
FIG. 8. Time records of the instantaneous Richardson number Ri_{inst}. The experiments with Ri_{mean} = (a) 0.5, (b) 1, (c) 2, and (d) 4. The dashed horizontal lines correspond to the critical Richardson number of $Ri_{cr} = 1/4$.

Fernandes and Krishnamurti 2010; Kimura and Smyth 2011), and it is comforting to see that the conclusion holds in a more realistic time-dependent environment. Simulations offer no evidence for

isotropic suppression of fingers by temporal changes in the direction of the background flow.

2) The vertical double-diffusive transport of heat and salt in the time-dependent GM-based shear is
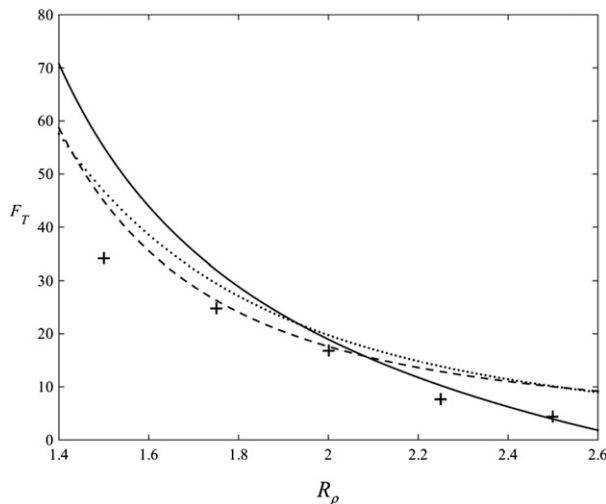
FIG. 9. Nondimensional heat fluxes from the experiments with the stochastic shear (indicated by plus signs) are plotted as a function of the density ratio. Also shown are the flux laws developed for two-dimensional nonsheared salt fingers in Stern et al. (2001), Simeonov and Stern (2004), and Radko (2014). These parameterizations are indicated by dashed, dotted, and solid curves, respectively.

reduced by approximately a factor of 2 relative to the nonsheared 3D simulations and is close to the corresponding 2D simulations. Several studies have noted that while the presence/absence of stable shears does significantly alter the finger-driven transport (e.g., Kimura and Smyth 2007), the variation of fluxes with the strength of shear is weak (Fernandes and Krishnamurti 2010; Kimura et al. 2011). The relative independence of fluxes from the shear strength is consistent with our interpretation of shear as mostly an agent for two-dimensionalizing salt fingers. When fingers are aligned in the direction of shear, they effectively cease the interaction with shear flow (Radko 2013). Thus, while the presence of a dynamically stable shear matters, its strength generally does not.

3) Finger-driven fluxes can be reduced by the interaction with turbulence generated by Kelvin–Helmholtz instabilities of internal waves (e.g., Smyth and Kimura 2011). However, when dynamic destabilization occurs only in a small fraction of the time record, which is representative of open-ocean conditions, the impact on salt fingers is moderate. The double-diffusive T–S fluxes remain close to their two-dimensional non-sheared counterparts.

4) The dynamically significant component of shear is near inertial. The magnitudes of high-frequency ($\omega \sim N$) and intermediate-frequency ($f \ll \omega \ll N$) components are too low to significantly affect the finger dynamics and transport characteristics. In this

regard, it should be mentioned that, if anything, the GM spectrum tends to underestimate the amplitudes of near-inertial waves (Fu 1981; Garrett 2001). Therefore, in the ocean, near-inertial components could play an even larger role in terms of controlling double-diffusive transport.

It is important to emphasize that all foregoing conclusions are based on simulations forced by the GM-based shears and therefore they may not be applicable to regimes in which the wave environment does not conform to the Garrett–Munk spectrum. For instance, the key feature of this spectrum is low amplitude of high-frequency components, which is generally supported by observations (e.g., Polzin and Lvov 2011). However, this assumption may be violated in regions strongly unstable with respect to Stern's (1969) collective instability. Collective instability results in the spontaneous generation of relatively high-frequency gravity waves due to their interaction with salt fingers (e.g., Stern et al. 2001; Stern and Simeonov 2002; Radko and Stern 2011). Since the present approach does not take into account possible wave–finger feedbacks, the possibility exists that the importance of high-frequency components in such regions could have been underestimated.

One of the important practical implications of our study is the opportunity it provides for representing finger-driven transport in large-scale numerical and analytical models. A major obstacle for developing such parameterizations was the uncertainty with regard to the impact of shear on salt fingers (e.g., Schmitt 1994, 2003). Systematic measurements of finescale shears are unavailable in most regions of the World Ocean, and the internal wave environment is not well captured by numerical climate models. In this regard, our finding that double-diffusive transport in the stochastic wave environment can be approximated by the corresponding 2D nonsheared fluxes is highly valuable. It implies that the assessment of fluxes does not require direct knowledge of the local shear characteristics. These results open a simple pathway for representing finger-driven mixing based on two-dimensional DNS, parameterizations of which have already been developed and successfully tested (e.g., Stern et al. 2001; Simeonov and Stern 2004; Radko 2014).

REFERENCES

Colosi, J. A., and M. G. Brown, 1998: Efficient numerical simulation of stochastic internal-wave-induced sound-speed perturbation fields. *J. Acoust. Soc. Amer.*, **103**, 2232–2235, doi:10.1121/1.421381.

Fernandes, A. M., and R. Krishnamurti, 2010: Salt finger fluxes in a laminar shear flow. *J. Fluid Mech.*, **658**, 148–165, doi:10.1017/S0022112010001588.

Fu, L.-L., 1981: Observations and models of inertial waves in the deep ocean. *Rev. Geophys.*, **19**, 141–170, doi:10.1029/RG019i001p00141.

Garrett, C., 2001: What is the ''near-inertial'' band and why is it different from the rest of the internal wave spectrum? *J. Phys. Oceanogr.*, **31**, 962–971, doi:10.1175/1520-0485(2001)031<0962:WITNIB>2.0.CO;2.

——, and W. Munk, 1972: Space-time scales of ocean internal waves. *Geophys. Fluid Dyn.*, **3**, 225–264, doi:10.1080/03091927208236082.

Holyer, J. Y., 1984: The stability of long, steady, two-dimensional salt fingers. *J. Fluid Mech.*, **147**, 169–185, doi:10.1017/S0022112084002044.

Kimura, S., and W. D. Smyth, 2007: Direct numerical simulation of salt sheets and turbulence in a double-diffusive shear layer. *Geophys. Res. Lett.*, **34**, L21610, doi:10.1029/2007GL031935.

——, and ——, 2011: Secondary instability of salt sheets. *J. Mar. Res.*, **69**, 57–77, doi:10.1357/002224011798147624.

——, ——, and E. Kunze, 2011: Turbulence in a sheared, salt-fingering-favorable environment: Anisotropy and effective diffusivities. *J. Phys. Oceanogr.*, **41**, 1144–1159, doi:10.1175/2011JPO4543.1.

Kunze, E., 1987: Limits on growing, finite length salt fingers: A Richardson number constraint. *J. Mar. Res.*, **45**, 533–556, doi:10.1357/002224087788326885.

——, 1990: The evolution of salt fingers in inertial wave shear. *J. Mar. Res.*, **48**, 471–504, doi:10.1357/002224090784984696.

——, 1994: A proposed constraint for salt fingers in shear. *J. Mar. Res.*, **52**, 999–1016, doi:10.1357/0022240943076867.

Linden, P. F., 1974: Salt fingers in a steady shear flow. *Geophys. Fluid Dyn.*, **6**, 1–27, doi:10.1080/03091927409365785.

Monin, A. S., and R. V. Ozmidov, 1985: *Turbulence in the Ocean.* Reidel, 247 pp.

Munk, W., 1981: Internal waves and small scale processes. *Evolution in Physical Oceanography*, F. Warren and C. Wunsch, Eds., MIT Press, 236–263.

Polzin, K. L., and Y. V. Lvov, 2011: Toward regional characterizations of the oceanic internal wavefield. *Rev. Geophys.*, **49**, RG4003, doi:10.1029/2010RG000329.

——, E. Kunze, J. M. Toole, and R. W. Schmitt, 2003: The partition of fine-scale energy into internal waves and geostrophic motions. *J. Phys. Oceanogr.*, **33**, 234–248, doi:10.1175/1520-0485(2003)033<0234:TPOFEI>2.0.CO;2.

Radko, T., 2003: A mechanism for layer formation in a double-diffusive fluid. *J. Fluid Mech.*, **497**, 365–380, doi:10.1017/S0022112003006785.

——, 2013: *Double-Diffusive Convection.* Cambridge University Press, 344 pp.

——, 2014: Applicability and failure of the flux-gradient laws in double-diffusive convection. *J. Fluid Mech.*, **750**, 33–72, doi:10.1017/jfm.2014.244.

——, and M. E. Stern, 2011: Finescale instabilities of the double-diffusive shear flow. *J. Phys. Oceanogr.*, **41**, 571–585, doi:10.1175/2010JPO4459.1.

——, and D. P. Smith, 2012: Equilibrium transport in double-diffusive convection. *J. Fluid Mech.*, **692**, 5–27, doi:10.1017/jfm.2011.343.

Schmitt, R. W., 1994: Double diffusion in oceanography. *Annu. Rev. Fluid Mech.*, **26**, 255–285, doi:10.1146/annurev.fl.26.010194.001351.

——, 2003: Observational and laboratory insights into salt finger convection. *Prog. Oceanogr.*, **56**, 419–433, doi:10.1016/S0079-6611(03)00033-8.

Simeonov, J., and M. E. Stern, 2004: Double-diffusive intrusions on a finite-width thermohaline front. *J. Phys. Oceanogr.*, **34**, 1723–1740, doi:10.1175/1520-0485(2004)034<1723:DIOAFT>2.0.CO;2.

Smyth, W. D., and S. Kimura, 2011: Mixing in a moderately sheared salt-fingering layer. *J. Phys. Oceanogr.*, **41**, 1364–1384, doi:10.1175/2010JPO4611.1.

Stellmach, S., A. Traxler, P. Garaud, N. Brummell, and T. Radko, 2011: Dynamics of fingering convection. Part 2: The formation of thermohaline staircases. *J. Fluid Mech.*, **677**, 554–571, doi:10.1017/jfm.2011.99.

Stern, M. E., 1969: Collective instability of salt fingers. *J. Fluid Mech.*, **35**, 209–218, doi:10.1017/S0022112069001066.

——, and J. Simeonov, 2002: Internal wave overturns produced by salt fingers. *J. Phys. Oceanogr.*, **32**, 3638–3656, doi:10.1175/1520-0485(2002)032<3638:IWOPBS>2.0.CO;2.

——, T. Radko, and J. Simeonov, 2001: 3D salt fingers in an unbounded thermocline with application to the Central Ocean. *J. Mar. Res.*, **59**, 355–390.

St. Laurent, L., and R. W. Schmitt, 1999: The contribution of salt fingers to vertical mixing in the North Atlantic tracer release experiment. *J. Phys. Oceanogr.*, **29**, 1404–1424, doi:10.1175/1520-0485(1999)029<1404:TCOSFT>2.0.CO;2.

Sun, H., and E. Kunze, 1999: Internal wave–wave interactions. Part I: The role of internal wave vertical divergence. *J. Phys. Oceanogr.*, **29**, 2886–2904, doi:10.1175/1520-0485(1999)029<2886:IWWIPI>2.0.CO;2.

Wells, M. G., and R. W. Griffiths, 2003: Interaction of salt finger convection with intermittent turbulence. *J. Geophys. Res.*, **108**, 3080, doi:10.1029/2002JC001427.

You, Y., 2002: A global ocean climatological atlas of the Turner angle: Implications for double-diffusion and water mass structure. *Deep-Sea Res.*, **49**, 2075–2093, doi:10.1016/S0967-0637(02)00099-7.